

Article

Sound Transmission Loss of a Honeycomb Sandwich Cylindrical Shell with Functionally Graded Porous Layers

Chanachai Thongchom ¹, Thira Jearsiripongkul ², Nima Refahati ³, Peyman Roudgar Saffari ⁴,
Pouyan Roodgar Saffari ^{1,*}, Sayan Sirimontree ¹ and Suraparb Keawsawasvong ^{1,*}

¹ Department of Civil Engineering, Faculty of Engineering, Thammasat School of Engineering, Thammasat University, Pathumthani 12120, Thailand; tchanach@engr.tu.ac.th (C.T.); ssayan@engr.tu.ac.th (S.S.)

² Department of Mechanical Engineering, Faculty of Engineering, Thammasat School of Engineering, Thammasat University, Pathumthani 12120, Thailand; jthira@engr.tu.ac.th

³ Department of Mechanical Engineering, Damavand Branch, Islamic Azad University, Damavand P.O. Box 3971878911, Iran; refahati@damavandiau.ac.ir

⁴ Department of Mechanical Engineering, Adiban Institute of Higher Education, Garmsar P.O. Box 3588143112, Iran; saffari.p86@gmail.com

* Correspondence: pouyan.safari31@gmail.com (P.R.S.); ksurapar@engr.tu.ac.th (S.K.)

Abstract: To examine the acousto-structural behavior of a sandwich cylindrical shell benefiting from hexagonal honeycomb structures in its core and functionally graded porous (FGP) layers on its outer and inner surfaces, a comprehensive study based on an analytical model which also considers the effect of an external flow is conducted. A homogenous orthotropic model is used for the honeycomb core while its corresponding material features are found from the modified Gibson's equation. The distribution pattern of FGP parts is either even or logarithmic-uneven, and a special rule-of-mixture relation governs their properties. Based on the first-order shear deformation theory (FSDT), Hamilton's principle is exploited to derive the final coupled vibro-acoustic equations, which are then solved analytically to allow us to calculate the amount of sound transmission loss (STL) through the whole structure. This acoustic property is further investigated in the frequency domain by changing a set of parameters, i.e., Mach number, wave approach angle, structure's radius, volume fraction, index of functionally graded material (FGM), and different honeycomb properties. Overall, good agreement is observed between the result of the present study and previous findings.

Keywords: honeycomb sandwich cylindrical shells; sound transmission loss; external flow; functionally graded porous materials; first-order shear deformation theory



Citation: Thongchom, C.; Jearsiripongkul, T.; Refahati, N.; Roudgar Saffari, P.; Roodgar Saffari, P.; Sirimontree, S.; Keawsawasvong, S. Sound Transmission Loss of a Honeycomb Sandwich Cylindrical Shell with Functionally Graded Porous Layers. *Buildings* **2022**, *12*, 151. <https://doi.org/10.3390/buildings12020151>

Academic Editors: Daniele Zulli and Valeria Settmi

Received: 3 January 2022

Accepted: 28 January 2022

Published: 1 February 2022

Publisher's Note: MDPI stays neutral with regard to jurisdictional claims in published maps and institutional affiliations.



Copyright: © 2022 by the authors. Licensee MDPI, Basel, Switzerland. This article is an open access article distributed under the terms and conditions of the Creative Commons Attribution (CC BY) license (<https://creativecommons.org/licenses/by/4.0/>).

1. Introduction

Sandwich structures are multilayer physical members composed of two stiff face sheets bonded to a core layer. Core layers usually consist of metallic and non-metallic honeycomb core, open and closed cell foams, and balsa wood [1–5]. One of the promising ways to reduce material cost and weight is to utilize honeycomb structures of various shapes. Most frequently, such structures are employed instead of or in combination with plates and shells, especially as a lightweight core. There have been several applications of honeycomb materials in various engineering fields, corroborating their numerous benefits including high specific strength/stiffness, incredibly lower weight, energy damping, and proper stability. However, their vibration characteristics, especially in combination with shells and plates, still need further evaluation. Li and Jin [6] investigated the natural frequencies of symmetric rectangular honeycomb panels under clamped and simply supported boundary conditions, applying corrected Gibson formula and third-order shear deformation theory (TSDT). Li et al. [7] analyzed geometrically nonlinear free vibration of symmetric honeycomb sandwich panels considering simply supported boundary condition

utilizing homotopy analysis technique and TSDT. Duc et al. [8] analytically studied nonlinear dynamic behavior of sandwich composite cylindrical panels with auxetic honeycomb core layer subjected to blast, damping, and mechanical loads. Duc et al. [9] employed FSDT to calculate the dynamic response of composite double curved shallow shells with negative Poisson's ratios in auxetic honeycombs core layer. Li et al. [10] predicated the natural frequencies of a thin-walled hexagonal honeycomb sandwich cylindrical shell according to Flügge's shell theory, and used finite element method (FEM) and experimental results to validate their models. Eipakchi et al. [11] presented a mathematical process to calculate the critical velocities, dynamic response, and the natural frequencies of composite cylindrical shells with auxetic honeycombs core layer under a moving pressure. Quyen et al. [12] carried out the nonlinear dynamic response of a honeycomb sandwich cylindrical panel on visco-Pasternak substrates under thermal and blast loading.

A shell structure, usually defined as a thin, curved plate, is a generally lightweight element that can be used in different sizes and applications. The main body of nearly all vehicles is built from such shell elements, and these structures have become an indispensable part of other advanced technologies such as reactors and gigantic telescopes. Unsurprisingly, they undergo large loads in different environments and scenarios, especially when placed inside a fluid or when facing aerodynamic loads. The resulting vibrations can specifically create a strong noise in the surroundings, and are thus required to be fully investigated under such circumstances [13–17]. In this regard, forced and free vibrations of cylindrical shells and mechanical properties of polymer based nanocomposite have been thoroughly investigated in the past, as in the works of [18–24].

Functionally graded materials (FGMs) are generally characterized by the gradual changes of composition and structure over volume, thus offering different properties on different sides of the specimen [25–30]. They have shown promising results in mitigating common issues found in conventional laminated composites such as interfacial debonding and matrix cracking while finding their way into different industries. These materials can be employed in different arrangements, one of which is an FGM sandwich structure formed around a core layer and covered by external/internal faces. This straightforward configuration is easy to manufacture and offers various improvements over traditional FGMs, including better thermal protection and sound absorption. Nevertheless, accurate models are necessary to analyze them in different applications [31–33]. Loy et al. [34] studied the effect of constituent volume fractions of FGMs on the natural frequencies of a cylindrical shell using Love's shell theory and Rayleigh-Ritz method. Pradhan et al. [35] used volume fraction power law distribution to analyze the free vibration of FGM cylindrical shells under various boundary conditions. Based on the FSDT in conjunction with the wave based method (WBM), Liu et al. [36] investigated the effect of material gradient index on the natural frequencies of FGM cylindrical shells. The influence of the nonlinear temperature variations and porosity volume fraction, and constituent volume on the natural frequencies of FGM cylindrical shells are presented by Wang et al. [37]. Baghlani et al. [38] developed and suggested a semi-analytical method to compute the natural frequency of eccentrically stiffened FGM shells considering fluid-structure interaction and higher-order shear deformation theory. Sofiyev [39] investigated the dynamic behavior of the infinitely-long FGM cylindrical shells under moving loads. Baghbadorani and Kiani [40] performed research on the behavior of a cylindrical shell made of a composite material reinforced with graphene platelets employing FSDT and Halpin-Tsai micro-mechanical. Nguyen et al. [41] proposed a semi analytical method to study the nonlinear asymmetric vibration of corrugated sandwich FGM cylindrical shells containing fluid subjected to harmonic radial load. Ni et al. [42] investigated the effects of magneto-electro-thermal loadings and material properties on the free vibration characteristics of FGM cylindrical shells. Cong and Duc [43] used the Galerkin method and FSDT to predict the nonlinear thermo-buckling and post-buckling behavior of eccentrically stiffened FGM double curved shallow auxetic honeycomb sandwich shells.

Another aspect of FGMs worthy of mention is the formation of voids owing to the differences in solidification temperature when sintering them, as discovered by Rodriguez-Castro [44] through a series scanning electron microscopy studies. The porosity level greatly affects the mechanical behavior of FGMs, and should thus be precisely characterized to be able to predict the dynamic response of FGM-incorporated structures. Wang [45] performed the free vibration of a FGM porous cylindrical shell under different sets of immovable boundary conditions using sinusoidal shear deformation theory. Cuong-Le et al. [46] studied the elastic instability and free vibration of annular plate, cylindrical and conical shell made of FGM porous rock materials using isogeometric analysis (IGA). They assumed that according to a power-law model, the remarkable material properties are associated with the porosity volume fraction and are considered to be constantly changeable through the thickness direction. Shahgholian et al. [47] presented buckling behavior a porous nanocomposite cylindrical shell reinforced with graphene platelets (GPLs) based on the FSDT and Halpin-Tsai micromechanics approach. Ghadiri and SafarPour [48] used modified couple stress theory in conjunction with FSDT to investigate the free vibration analysis of a FGM porous cylindrical microshell under a thermal environment. Keleshteri and Jelovica [49] denoted that both porosity coefficient and porosity distribution have a notable effect on the nonlinear natural frequencies of FG porous cylindrical panels using FSDT and generalized differential quadrature method (GDQM). Li et al. [50] investigated the thermal vibration problem of an FG porous stepped cylindrical shell applying characteristic orthogonal polynomials and FSDT.

Sound transmission through different objects in another interesting area of study for vibro-acoustic engineers [51]. More specifically, STL determines the amount of sound (usually in decibels/dB) isolated by a certain structure, and is considered to be an important quantity when acoustic effects are not negligible. Generally, a plethora of analytical equations have been proposed to obtain the sound transmission characteristics of most common structures, such as fuselages and building walls as in the study by Heckl [52]. A major hindrance, however, to implement these equations is to find their exact solutions, hence giving rise to various approximate approaches over the course of time. Pellicier and Trompette [53] provided a comprehensive review of such techniques. Ramezani and Talebitooti [54] used the three different distribution models, including power-law, sigmoid, and exponential types, to predict STL across a double-walled FGM porous sandwich cylindrical shell. Daneshjou et al. [55] presented STL of a thick-walled cylindrical shell based on three dimensional (3-D) theory of elasticity. Oliazadeh and Farshidianfar [56] applied Donnell's shell theory to analyze STL through double- and triple-walled cylindrical shells. Ahmadi et al. [57] analyzed the effect of different models of carbon nanotube distribution on the variation of acoustic transmission of FGM carbon nanotube-reinforced composite cylindrical shells using FSDT. Hasheminejad et al. [58] performed STL through a sandwich cylindrical shell with electrorheological fluid core. Fu et al. [59] indicated the effects of gradient index, porosity volume fraction, and porosity distribution type on the variations of STL of a FG porous cylindrical shell under nonlinear thermal loading. Hasheminejad and Jamalpoor [60] improved the diffuse STL across a smart hybrid double concentric sandwich circular cylindrical shell structure under internal and external air gap mean flows using multi-input multi-output (MIMO) sliding mode control (SMC). According to the hyperbolic tangent shear deformation assumption, Li et al. [61] calculated the natural frequencies and STL of FG honeycomb sandwich plates.

To the best of authors' knowledge, no study has considered the sound transmission and wave propagation of FGM-incorporated honeycomb sandwich cylindrical shells until now. To fill this gap, this paper examines the behavior of an incident sound wave passing through a honeycomb sandwich shell filled with air and benefiting from FGP layers. For a more realistic evaluation, the whole structure is assumed to be located in fluid flow, and the structural response is analyzed via the FSDT. A power law model is necessary to describe the varying material properties caused by two porosity patterns (i.e., even distribution and logarithmic-uneven pattern). For the simulation part of this study, the honeycomb core is

represented by a homogenous orthotropic material whose different features are explained via a modified Gibson's equation.

The outline of the paper is as follows. Section 2 expresses the acoustic equation of fluids and the governing equations, whereas in Section 3 the STL is defined. Finally, comparisons and parametric results to study the acousto-structural behavior of a honeycomb sandwich cylindrical shell with FGP layers are proposed in Section 4.

2. Mathematical Model

Figure 1 shows the schematic of the problem at hand. The honeycomb core of the sandwich cylindrical shell has a radius of R and thickness of H . The hexagonal cells are characterized by t_c , l_c , and θ_c . The exterior and the interior of this core are enclosed by porous layers of FGP materials, each having a thickness of h . The external FGP layer also faces a steady fluid flow, which is air in this case. Finally, the hollow section of the sandwich structure houses air, with the characteristic impedance of (ρ_0, c_0) . In addition, a steady flow of air passes over the structure at the velocity \mathcal{V} .

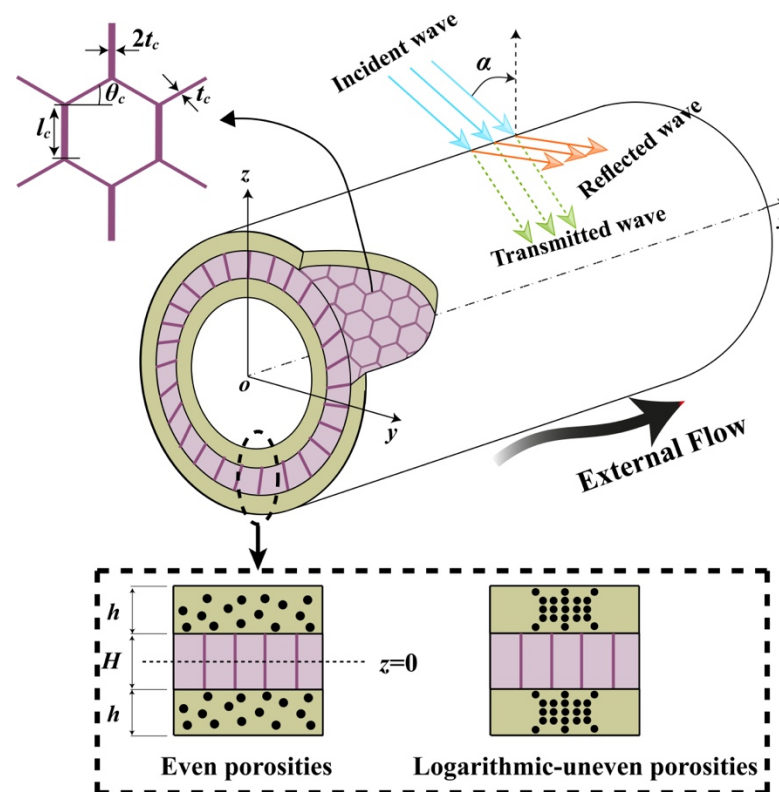


Figure 1. The schematic of a honeycomb sandwich cylindrical shell with FGP layers under incidence wave.

2.1. Acoustic Equation of Fluids

The wave equation in the external fluid medium (incident region) considering an airflow with constant velocity (\mathcal{V}) can be expressed as [62]

$$c_0^2 \nabla^2 (p_1^I + p_1^R) + \left(\frac{\partial}{\partial t} + \mathcal{V} \cdot \nabla \right)^2 (p_1^I + p_1^R) = 0, \quad (1)$$

where $\nabla^2 = \frac{1}{r} \frac{\partial}{\partial r} \left(r \frac{\partial}{\partial r} \right) + \frac{1}{r^2} \frac{\partial^2}{\partial \theta^2} + \frac{\partial^2}{\partial x^2}$ refers to the Laplacian operator in the cylindrical coordinate system. Furthermore p_1^I and p_1^R are the acoustic pressures associated with the

incident and reflected waves, respectively. The acoustic wave equation in the internal fluid medium (transmitted region) is indicated as

$$c_0^2 \nabla^2 p_2^T = \frac{\partial^2}{\partial t^2} p_2^T, \quad (2)$$

where p_2^T describes the transmitted wave. For cylindrical coordinate system, the terms of time-harmonic pressure waves are defined as [63]

$$\begin{aligned} p_1^I(r, \theta, x, t) &= p_0 e^{i(\Omega t - k_x x)} \sum_{n=0}^{\infty} \varepsilon_n (-i)^n J_n(k_{1r} r) \cos(n\theta), \\ p_1^R(r, \theta, x, t) &= e^{i(\Omega t - k_x x)} \sum_{n=0}^{\infty} \widehat{P}_{1n}^R H_n^{(2)}(k_{1r} r) \cos(n\theta), \\ p_2^T(r, \theta, x, t) &= e^{i(\Omega t - k_x x)} \sum_{n=0}^{\infty} \widehat{P}_{2n}^T H_n^{(1)}(k_{3r} r) \cos(n\theta), \end{aligned} \quad (3)$$

It should be noted that $\varepsilon_0 = 1$, $\varepsilon_n = 2(n \geq 1)$, p_0 expresses the amplitude of pressure of the incident wave, Ω displays the angular frequency, $i = \sqrt{-1}$, J_n signifies the cylindrical Bessel function of the first kind and n -th order, and $H_n^{(1)}$ and $H_n^{(2)}$ indicate, respectively, the cylindrical Hankel functions of the first and second kinds. Also, $(\widehat{P}_{1n}^R, \widehat{P}_{2n}^T, \widehat{P}_{2n}^R, \widehat{P}_{3n}^T)$ are unknown complex coefficients. Furthermore, the radial and axial components of the wavenumbers are stated as

$$\begin{aligned} k_x &= k_1 \sin \alpha, \quad k_{1r} = k_1 \cos \alpha = [k_1^2 - k_x^2]^{1/2}, \\ k_{2r} &= \sqrt{k_2^2 - k_x^2}, \quad k_1 = \Omega / [c_0(1 + M \sin \alpha)], \quad k_2 = \Omega / c_0, \end{aligned} \quad (4)$$

in which $M = \mathcal{V} / c_0$ refers to the Mach number of the external flow.

2.2. Equations of Motion

Despite the generally acceptable results obtained from FSDT, it poses certain difficulties for some thick laminates in sandwich configurations whose transverse shear modulus is not large enough [64,65]. As varying transverse shear strains are not inherently implemented in this approach, it is assumed that virtual transverse shear strains are presented on the surfaces of sandwich structures. To express the displacement fields under such assumptions, one can write [66]

$$\begin{aligned} u(x, \theta, z, t) &= U(x, \theta, t) + z\phi_x(x, \theta, t), \\ v(x, \theta, z, t) &= V(x, \theta, t) + z\phi_\theta(x, \theta, t), \\ w(x, \theta, z, t) &= W(x, \theta, t), \end{aligned} \quad (5)$$

where U and V describe the in-plane deflections of the mid-surface along x and θ directions, respectively. Also, the transverse deflection of the structure is expressed with W . Furthermore, the rotation angles of the middle plane along θ and x directions are signified by ϕ_θ and ϕ_x , respectively. The displacement and rotation terms are stated as [67,68]

$$\begin{aligned} \langle U, W, \phi_x \rangle &= \sum_{n=0}^{\infty} e^{i(\Omega t - k_x x)} \langle \overline{U}, \overline{W}, \overline{\phi}_x \rangle \cos(n\theta), \\ \langle V, \phi_\theta \rangle &= \sum_{n=0}^{\infty} e^{i(\Omega t - k_x x)} \langle \overline{V}, \overline{\phi}_\theta \rangle \sin(n\theta), \end{aligned} \quad (6)$$

in which $\langle \overline{U}, \overline{\phi}_x, \overline{V}, \overline{\phi}_\theta, \overline{W} \rangle$ denote the unknown modal factors. However, the strain components in terms of the curvature and mid-surface strain of the sandwich shell are written as follows

$$\begin{aligned} \varepsilon_{xx} &= \frac{\partial U}{\partial x} + z \frac{\partial \phi_x}{\partial x}, \\ \varepsilon_{\theta\theta} &= \frac{1}{R} \frac{\partial V}{\partial \theta} + \frac{z}{R} \frac{\partial \phi_\theta}{\partial \theta} + \frac{W}{R}, \\ \gamma_{x\theta} &= \frac{\partial V}{\partial x} + \frac{1}{R} \frac{\partial U}{\partial \theta} + z \left(\frac{1}{R} \frac{\partial \phi_x}{\partial \theta} + \frac{\partial \phi_\theta}{\partial x} \right), \\ \gamma_{\theta z} &= \phi_\theta + \frac{1}{R} \frac{\partial W}{\partial \theta} - \frac{V}{R}, \\ \gamma_{xz} &= \frac{\partial W}{\partial x} + \phi_x. \end{aligned} \quad (7)$$

in which normal and shear strains are signified by $(\varepsilon_{xx}, \varepsilon_{\theta\theta})$ and $(\gamma_{x\theta}, \gamma_{xz}, \gamma_{\theta z})$, respectively. The stress-strain relation for inner and outer FGP layers can be expressed as

$$\begin{bmatrix} \sigma_{xx}^{T,B} \\ \sigma_{\theta\theta}^{T,B} \\ \tau_{x\theta}^{T,B} \\ \tau_{\theta z}^{T,B} \\ \tau_{xz}^{T,B} \end{bmatrix} = \begin{bmatrix} \frac{E^{T,B}(z)}{1-\vartheta^{T,B}(z)\vartheta^{T,B}(z)} & \frac{\vartheta(z)E^{T,B}(z)}{1-\vartheta^{T,B}(z)\vartheta^{T,B}(z)} & 0 & 0 & 0 \\ \frac{\vartheta^{T,B}(z)E^{T,B}(z)}{1-\vartheta^{T,B}(z)\vartheta^{T,B}(z)} & \frac{E^{T,B}(z)}{1-\vartheta^{T,B}(z)\vartheta^{T,B}(z)} & 0 & 0 & 0 \\ 0 & 0 & \frac{E^{T,B}(z)}{2(1+\vartheta^{T,B}(z))} & 0 & 0 \\ 0 & 0 & 0 & \frac{E^{T,B}(z)}{2(1+\vartheta^{T,B}(z))} & 0 \\ 0 & 0 & 0 & 0 & \frac{E^{T,B}(z)}{2(1+\vartheta^{T,B}(z))} \end{bmatrix} \begin{bmatrix} \varepsilon_{xx} \\ \varepsilon_{\theta\theta} \\ \gamma_{x\theta} \\ \gamma_{\theta z} \\ \gamma_{xz} \end{bmatrix}, \quad (8)$$

where the superscript T and B are the top and bottom layers, respectively. Furthermore, E and ϑ refer to the Young's modulus and Poisson's ratio, respectively. To achieve FG-like properties, the bottom and top surfaces of the sandwich structure are purely made from metal and ceramic, respectively. As already described, two porosity distribution patterns, namely even and logarithmic-uneven, were considered for this study. Accordingly, the corresponding values of elastic modulus, mass density, and Poisson's ratio based on the rule of mixture are described as [69]

Even porosity dispersion:

$$\begin{aligned} E^T(z) &= (E_c - E_m)(z/h - H/2h)^p + E_m - 0.5\zeta(E_c + E_m), \\ \rho^T(z) &= (\rho_c - \rho_m)(z/h - H/2h)^p + \rho_m - 0.5\zeta(\rho_c + \rho_m), \\ \vartheta^T(z) &= (\vartheta_c - \vartheta_m)(z/h - H/2h)^p + \vartheta_m - 0.5\zeta(\vartheta_c + \vartheta_m), \\ E^B(z) &= (E_c - E_m)(z/h + H/2h)^p + E_m - 0.5\zeta(E_c + E_m), \\ \rho^B(z) &= (\rho_c - \rho_m)(z/h + H/2h)^p + \rho_m - 0.5\zeta(\rho_c + \rho_m), \\ \vartheta^B(z) &= (\vartheta_c - \vartheta_m)(z/h + H/2h)^p + \vartheta_m - 0.5\zeta(\vartheta_c + \vartheta_m), \end{aligned} \quad (9)$$

Logarithmic uneven porosity dispersion:

$$\begin{aligned} E^T(z) &= (E_c - E_m)(z/h - H/2h)^p + E_m - \log(1 + 0.5\zeta) \left(1 - 2\frac{|z|}{h}\right) (E_c + E_m), \\ \rho^T(z) &= (\rho_c - \rho_m)(z/h - H/2h)^p + \rho_m - \log(1 + 0.5\zeta) \left(1 - 2\frac{|z|}{h}\right) (\rho_c + \rho_m), \\ \vartheta^T(z) &= (\vartheta_c - \vartheta_m)(z/h - H/2h)^p + \vartheta_m - \log(1 + 0.5\zeta) \left(1 - 2\frac{|z|}{h}\right) (\vartheta_c + \vartheta_m), \\ E^B(z) &= (E_c - E_m)(z/h + H/2h)^p + E_m - \log(1 + 0.5\zeta) \left(1 - 2\frac{|z|}{h}\right) (E_c + E_m), \\ \rho^B(z) &= (\rho_c - \rho_m)(z/h + H/2h)^p + \rho_m - \log(1 + 0.5\zeta) \left(1 - 2\frac{|z|}{h}\right) (\rho_c + \rho_m), \\ \vartheta^B(z) &= (\vartheta_c - \vartheta_m)(z/h + H/2h)^p + \vartheta_m - \log(1 + 0.5\zeta) \left(1 - 2\frac{|z|}{h}\right) (\vartheta_c + \vartheta_m), \end{aligned} \quad (10)$$

where m and c signify metal and ceramic phases, respectively. Also, ρ is the mass density. The always-positive gradient index (p) is used in this study to determine the changes of a specific property in the thickness direction. The greater the gradient index, the more metallic the structure. Furthermore, ζ expresses the porosity coefficient. The classical constituent relations between stress and strain tensors for honeycomb core layer can be presented as:

$$\begin{bmatrix} \sigma_{xx}^C \\ \sigma_{\theta\theta}^C \\ \tau_{x\theta}^C \\ \tau_{\theta z}^C \\ \tau_{xz}^C \end{bmatrix} \begin{bmatrix} \frac{E_1^C}{1-\vartheta_{12}^C\vartheta_{21}^C} & \frac{\vartheta_{12}^C E_2^C}{1-\vartheta_{12}^C\vartheta_{21}^C} & 0 & 0 & 0 \\ \frac{\vartheta_{21}^C E_2^C}{1-\vartheta_{12}^C\vartheta_{21}^C} & \frac{E_2^C}{1-\vartheta_{12}^C\vartheta_{21}^C} & 0 & 0 & 0 \\ 0 & 0 & G_{12}^C & 0 & 0 \\ 0 & 0 & 0 & G_{12}^C & 0 \\ 0 & 0 & 0 & 0 & G_{12}^C \end{bmatrix} \begin{bmatrix} \varepsilon_{xx} \\ \varepsilon_{\theta\theta} \\ \gamma_{x\theta} \\ \gamma_{\theta z} \\ \gamma_{xz} \end{bmatrix}, \quad (11)$$

where G is the shear modulus. It should be noted that based on the corrected Gibson's formula, the corresponding material properties of honeycomb core layer are defined as [9,10]:

$$\begin{aligned}
 E_1^C &= E \left(\frac{t_c}{l_c} \right)^3 \frac{\cos \theta_c}{\left(\frac{H}{l_c} + \sin \theta_c \right) \sin^2 \theta_c} \left[1 - \cot^2 \theta_c \left(\frac{t_c}{l_c} \right)^2 \right], \\
 E_2^C &= E \left(\frac{t_c}{l_c} \right)^3 \frac{\frac{H}{l_c} + \sin \theta_c}{\cos^3 \theta_c} \left[1 - \left(\frac{H}{l_c} \sec^2 \theta_c + \tan^2 \theta_c \right) \left(\frac{t_c}{l_c} \right)^2 \right], \\
 \vartheta_{12}^C &= \frac{\cos^2 \theta_c}{\left(\frac{H}{l_c} + \sin \theta_c \right) \sin \theta_c} \left[1 - \csc^2 \theta_c \left(\frac{t_c}{l_c} \right)^2 \right], \\
 \vartheta_{21}^C &= \frac{\left(\frac{H}{l_c} + \sin \theta_c \right) \sin \theta_c}{\cos^2 \theta_c} \left[1 - \left(1 + \frac{H}{l_c} \right) \sec^2 \theta_c \left(\frac{t_c}{l_c} \right)^2 \right], \\
 G_{12}^C &= G_{12} \left(\frac{t_c}{l_c} \right)^3 \frac{\left(\frac{H}{l_c} + \sin \theta_c \right)}{\left(\frac{H}{l_c} \right)^2 \left(2 \frac{H}{l_c} + 1 \right) \cos \theta_c}, \\
 G_{23}^C &= G_{23} \frac{t_c}{l_c} \frac{1 + 2 \sin^2 \theta_c}{2 \cos \theta_c \left(\frac{H}{l_c} + \sin \theta_c \right)}, \\
 G_{13}^C &= G_{13} \frac{t_c}{l_c} \frac{\cos \theta_c}{\left(\frac{H}{l_c} + \sin \theta_c \right)}, \\
 \rho^C &= \rho \frac{t_c}{l_c} \frac{1 + \frac{H}{l_c}}{\left(\frac{H}{l_c} + \sin \theta_c \right) \cos \theta_c},
 \end{aligned} \tag{12}$$

The Hamilton's principle is applied to obtain the equilibrium equations of motion in the form [70]:

$$\int_0^t (\delta X_s + \delta X_f - \delta X_K) dt = 0, \tag{13}$$

where strain energy, the work done by external forces (the work applied by the incidence sound wave), and the kinetic energy are denoted with X_s , X_f , and X_K , respectively. The variation of kinetic energy of the sandwich honeycomb FGP shell is expressed as

$$\begin{aligned}
 \delta X_K &= \int_A \int_{-\frac{H}{2}-h}^{-\frac{H}{2}} \rho^B(z) (\dot{u} \delta \dot{u} + \dot{v} \delta \dot{v} + \dot{w} \delta \dot{w}) dz dA + \int_A \int_{-\frac{H}{2}}^{\frac{H}{2}} \rho^C (\dot{u} \delta \dot{u} + \dot{v} \delta \dot{v} + \dot{w} \delta \dot{w}) dz dS \\
 &+ \int_A \int_{\frac{H}{2}}^{\frac{H}{2}+h} \rho^T(z) (\dot{u} \delta \dot{u} + \dot{v} \delta \dot{v} + \dot{w} \delta \dot{w}) dz dS = \int_A \left[I_0 (\dot{U} \delta \dot{U} + \dot{V} \delta \dot{V} + \dot{W} \delta \dot{W}) \right. \\
 &\left. + I_1 (\dot{U} \delta \dot{\phi}_x + \dot{V} \delta \dot{\phi}_\theta + \dot{\phi}_x \delta \dot{U} + \dot{\phi}_\theta \delta \dot{V}) + I_2 (\dot{\phi}_x \delta \dot{\phi}_x + \dot{\phi}_\theta \delta \dot{\phi}_\theta) \right] dA,
 \end{aligned} \tag{14}$$

where A is the cross-sectional area, and:

$$\begin{aligned}
 I_0 &= \int_{-\frac{H}{2}-h}^{-\frac{H}{2}} \rho^B(z) dz + \int_{-\frac{H}{2}}^{\frac{H}{2}} \rho^C dz + \int_{\frac{H}{2}}^{\frac{H}{2}+h} \rho^T(z) dz, \\
 I_1 &= \int_{-\frac{H}{2}-h}^{-\frac{H}{2}} \rho^B(z) z dz + \int_{-\frac{H}{2}}^{\frac{H}{2}} \rho^C z dz + \int_{\frac{H}{2}}^{\frac{H}{2}+h} \rho^T(z) z dz, \\
 I_2 &= \int_{-\frac{H}{2}-h}^{-\frac{H}{2}} \rho^B(z) z^2 dz + \int_{-\frac{H}{2}}^{\frac{H}{2}} \rho^C z^2 dz + \int_{\frac{H}{2}}^{\frac{H}{2}+h} \rho^T(z) z^2 dz
 \end{aligned} \tag{15}$$

The variation of strain energy is presented as:

$$\begin{aligned}
 \delta X_s &= \int_A \int_{-\frac{H}{2}-h}^{-\frac{H}{2}} (\sigma_{xx}^B \delta \varepsilon_{xx} + \sigma_{\theta\theta}^B \delta \varepsilon_{\theta\theta} + \tau_{x\theta}^B \delta \gamma_{x\theta} + \tau_{xz}^B \delta \gamma_{xz} + \tau_{\theta z}^B \delta \gamma_{\theta z}) dz dA + \\
 &\int_A \int_{-\frac{H}{2}}^{\frac{H}{2}} (\sigma_{xx}^C \delta \varepsilon_{xx} + \sigma_{\theta\theta}^C \delta \varepsilon_{\theta\theta} + \tau_{x\theta}^C \delta \gamma_{x\theta} + \tau_{xz}^C \delta \gamma_{xz} + \tau_{\theta z}^C \delta \gamma_{\theta z}) dz dA + \\
 &\int_A \int_{\frac{H}{2}}^{\frac{H}{2}+h} (\sigma_{xx}^T \delta \varepsilon_{xx} + \sigma_{\theta\theta}^T \delta \varepsilon_{\theta\theta} + \tau_{x\theta}^T \delta \gamma_{x\theta} + \tau_{xz}^T \delta \gamma_{xz} + \tau_{\theta z}^T \delta \gamma_{\theta z}) dz dA.
 \end{aligned} \tag{16}$$

The forces are exerted to the cylinder stem from three sources: (1) the incident sound wave, (2) the reflected external sound pressure, and (3) the transmitted acoustic pressure

inside the cylindrical structure. In view of these three forces, one can calculate the work by external loads as:

$$\delta X_f = \int_A \Delta P \delta W dA, \quad \Delta P = (p_1^I + p_1^R) - (p_1^T) \quad (17)$$

By substituting Equations (14), (16), and (17) into (13) and performing some manipulations, the equations of motion for the sandwich honeycomb FGP shell can be derived as:

$$\begin{aligned} \delta U &: \frac{\partial N_{xx}}{\partial x} + \frac{1}{R} \frac{\partial N_{x\theta}}{\partial \theta} = I_0 \frac{\partial^2 U}{\partial t^2} + I_1 \frac{\partial^2 \phi_x}{\partial t^2}, \\ \delta V &: \frac{\partial N_{x\theta}}{\partial x} + \frac{1}{R} \frac{\partial N_{\theta\theta}}{\partial \theta} + \frac{Q_{\theta z}}{R} = I_0 \frac{\partial^2 V}{\partial t^2} + I_1 \frac{\partial^2 \phi_\theta}{\partial t^2}, \\ \delta W &: \frac{\partial Q_{xz}}{\partial x} + \frac{1}{R} \frac{\partial Q_{\theta z}}{\partial \theta} - \frac{N_{\theta\theta}}{R} = I_{01} \frac{\partial^2 W}{\partial t^2} - \Delta P, \\ \delta \phi_x &: \frac{\partial M_{xx}}{\partial x} + \frac{1}{R} \frac{\partial M_{x\theta}}{\partial \theta} - Q_{xz} = I_1 \frac{\partial^2 U}{\partial t^2} + I_2 \frac{\partial^2 \phi_x}{\partial t^2}, \\ \delta \phi_\theta &: \frac{1}{R} \frac{\partial M_{\theta\theta}}{\partial \theta} + \frac{\partial M_{x\theta}}{\partial x} - Q_{\theta z} = I_1 \frac{\partial^2 V}{\partial t^2} + I_2 \frac{\partial^2 \phi_\theta}{\partial t^2}, \end{aligned} \quad (18)$$

in which

$$\begin{aligned} [N_{xx}, M_{xx}] &= \int_{-\frac{H}{2}-h}^{-\frac{H}{2}} \sigma_{xx}^B [1, z] dz + \int_{-\frac{H}{2}}^{\frac{H}{2}} \sigma_{xx}^C [1, z] dz + \int_{\frac{H}{2}}^{\frac{H}{2}+h} \sigma_{xx}^T [1, z] dz, \\ [N_{x\theta}, M_{x\theta}] &= \int_{-\frac{H}{2}-h}^{-\frac{H}{2}} \tau_{x\theta}^B [1, z] dz + \int_{-\frac{H}{2}}^{\frac{H}{2}} \tau_{x\theta}^C [1, z] dz + \int_{\frac{H}{2}}^{\frac{H}{2}+h} \tau_{x\theta}^T [1, z] dz, \\ [N_{\theta\theta}, M_{\theta\theta}] &= \int_{-\frac{H}{2}-h}^{-\frac{H}{2}} \sigma_{\theta\theta}^B [1, z] dz + \int_{-\frac{H}{2}}^{\frac{H}{2}} \sigma_{\theta\theta}^C [1, z] dz + \int_{\frac{H}{2}}^{\frac{H}{2}+h} \sigma_{\theta\theta}^T [1, z] dz, \\ Q_{xz} &= k_s \left\{ \int_{-\frac{H}{2}-h}^{-\frac{H}{2}} \tau_{xz}^B dz + \int_{-\frac{H}{2}}^{\frac{H}{2}} \tau_{xz}^C dz + \int_{\frac{H}{2}}^{\frac{H}{2}+h} \tau_{xz}^T dz \right\}, \\ Q_{\theta z} &= k_s \left\{ \int_{-\frac{H}{2}-h}^{-\frac{H}{2}} \tau_{\theta z}^B dz + \int_{-\frac{H}{2}}^{\frac{H}{2}} \tau_{\theta z}^C dz + \int_{\frac{H}{2}}^{\frac{H}{2}+h} \tau_{\theta z}^T dz \right\}, \end{aligned} \quad (19)$$

where k_s is the shear correction coefficient, which depends on the material and geometric properties, boundary conditions, and forces. This study uses a shear correction coefficient of 5/6 as a reliable estimate, although it should be kept in mind that at small scales, this value turns out to be inaccurate. Lastly, replacing Equation (19) (considering relations (8) and (11)) into Equation (18), the equilibrium equations in terms of displacement and rotations are obtained and provided in Appendix A.

2.3. Continuity Conditions of Fluid/Structure

There is no need to consider a boundary condition along the z axis due to the infinite nature of the structure in this specific direction. The structural and acoustic domains are coupled in the following manner in the r direction [63,67]:

$$\begin{aligned} \frac{\partial}{\partial r} (p_1^I + p_1^R) \Big|_{r=R} &= -\rho_0 \left(\frac{\partial}{\partial t} + \nu \cdot \nabla \right)^2 W, \\ \frac{\partial}{\partial r} p_2^T \Big|_{r=R} &= -\rho_0 \frac{\partial^2 W}{\partial t^2}, \end{aligned} \quad (20)$$

By replacing Equations (3) and (6) into Equations (A1)–(A5), and Equation (20), after some manipulation, the equilibrium equations in a 7×7 matrix format can be obtained as:

$$\begin{bmatrix} 0 & 0 & Y_{1,3} & Y_{1,4} & Y_{1,5} & Y_{1,6} & Y_{1,7} \\ 0 & 0 & Y_{2,3} & Y_{2,4} & Y_{2,5} & Y_{2,6} & Y_{2,7} \\ Y_{3,1} & Y_{3,2} & Y_{3,3} & Y_{3,4} & Y_{3,5} & Y_{3,6} & Y_{3,7} \\ 0 & 0 & Y_{4,3} & Y_{4,4} & Y_{4,5} & Y_{4,6} & Y_{4,7} \\ 0 & 0 & Y_{5,3} & Y_{5,4} & Y_{5,5} & Y_{5,6} & Y_{5,7} \\ Y_{6,1} & 0 & 0 & 0 & Y_{6,5} & 0 & 0 \\ 0 & Y_{7,2} & 0 & 0 & Y_{7,5} & 0 & 0 \end{bmatrix} \begin{bmatrix} \bar{p}_{1n}^R \\ \bar{p}_{2n}^T \\ \bar{U} \\ \bar{V} \\ \bar{W} \\ \bar{\phi}_x \\ \bar{\phi}_\theta \end{bmatrix} = \begin{bmatrix} 0 \\ 0 \\ f_3 \\ 0 \\ 0 \\ f_6 \\ 0 \end{bmatrix}. \quad (21)$$

where parameters $Y_{i,j}$, f_3 , and f_6 are expressed in Appendix B.

3. STL

Dividing the transmitted to the incident acoustic powers (i.e., $\Pi^{\text{tr}}/\Pi^{\text{inc}}$) yields the transmission coefficient τ . The value of sound transmission loss is then obtained as

$$\begin{aligned} \text{STL} &= 10 \log \frac{1}{\tau}, \\ \tau &= \frac{\Pi^{\text{tr}}}{\Pi^{\text{inc}}}, \\ \Pi^{\text{tr}} &= \sum_n^{\infty} \frac{\pi R}{\varepsilon_n} \text{Re} \left[\widehat{P}_{2n}^{\text{T}} H_n^{(1)}(k_{2r} R) (i\omega \overline{W})^* \right], \\ \Pi^{\text{inc}} &= \frac{R p_0^2}{\rho c} \cos \alpha \end{aligned} \quad (22)$$

in which Re refers to the real part of the argument and the superscript “*” signifies the complex conjugate.

4. Numerical Results and Discussion

Before presenting the chief findings, a series of simplified cases are considered to demonstrate the validity of the developed procedure.

4.1. Mode Convergence

To show the effect of the number of modes on the convergence of results, a special case for the incoming wave angle of $\alpha = \pi/4$ is considered. According to Figure 2, satisfactory convergence at higher excitation frequencies necessitates a greater mode number. Different assumptions used for this investigation are presented in Table 1. Furthermore, hexagonal cells are assumed to be metal.

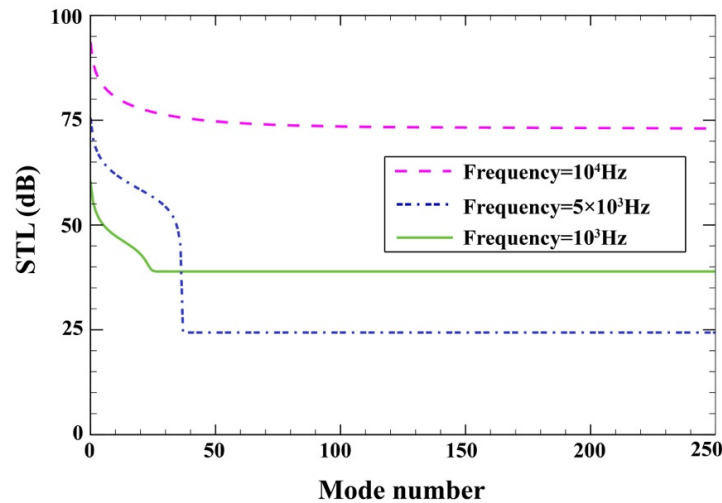


Figure 2. Mode convergence diagram.

Table 1. Material properties of the honeycomb sandwich cylindrical shell with FGP layers.

Properties	Alumina (Ceramic)	Steel (Metal)
Elastic (GPa)	$E_c = 390$	$E_m = 200$
Poisson's Ratio	$\nu_c = 0.24$	$\nu_m = 0.3$
Mass density (kg m^{-3})	$\rho_c = 3960$	$\rho_m = 7800$
Properties (Acoustic Medium)		Air
Sound Speed (m s^{-1})	$c_0 = 343$	
Mass density (kg m^{-3})	$\rho_0 = 1.21$	

4.2. Comparison Study

A series of comparisons are made here to show whether the developed procedure is accurate enough. As a first verification study, acoustic effects and honeycomb core layer were assumed to be nonexistent, then the natural frequencies (Hz) of the FGM cylindrical shell were calculated for different values of material gradient index based on the present formulation. The results alongside other numerical findings in Ref. [34] are provided in Table 2, demonstrating the acceptable accuracy of the present formulations.

Table 2. A comparative study of the natural frequencies of an FG cylindrical shell.

Power Law Index (p)	Mode Number (n)	Present	Ref. [24]
0	1	12.905	12.917
	2	31.578	31.603
	3	88.002	88.267
1	1	13.189	13.234
	2	32.267	32.418
	3	90.345	90.569
2	1	13.317	13.344
	2	32.549	32.683
	3	91.066	91.309

As a further verification targeting the structural part of the developed procedure, acoustic and FGP effects were neglected, and the natural frequencies (Hz) of the honeycomb sandwich cylindrical shell structure were extracted for different values of core-to-thickness ratios. As shown in Figure 3, the developed formulation almost matches the previous numerical findings in another study by Li et al. [10] (Flügge shell theory).

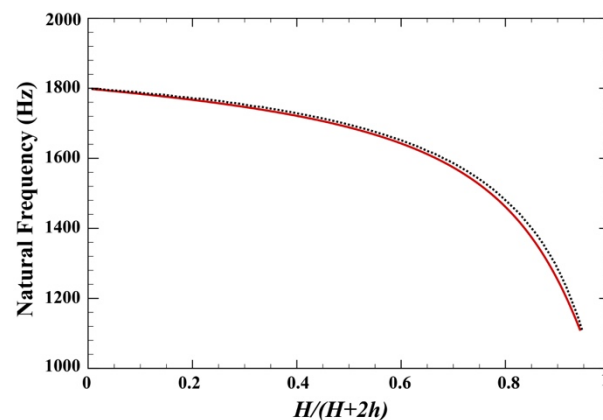


Figure 3. Comparison study of the natural frequencies (Hz) of the honeycomb sandwich cylindrical shell, red solid line: present, black dotted line: Ref [10].

Also, as shown in Figure 4a,b, for an elastic cylindrical shell, STL from an incident acoustic wave at $\alpha = \pi/4$ was found from the derived formulation, then compared with the results of 3D elasticity theory in Ref. [55] and those of an FSDT approach in Ref. [71] in the frequency domain for the properties mentioned in those studies. As another validation, for a simplified case of aluminum shell, a comparison with the present results based on the FSDT the classical shell theory was performed. STL was found for an incident wave angle at $\alpha = \pi/4$. As observed in Figure 4c, there is practically no difference between the findings of this study and those of a numerical method by Ref. [63] (classical shell theory).

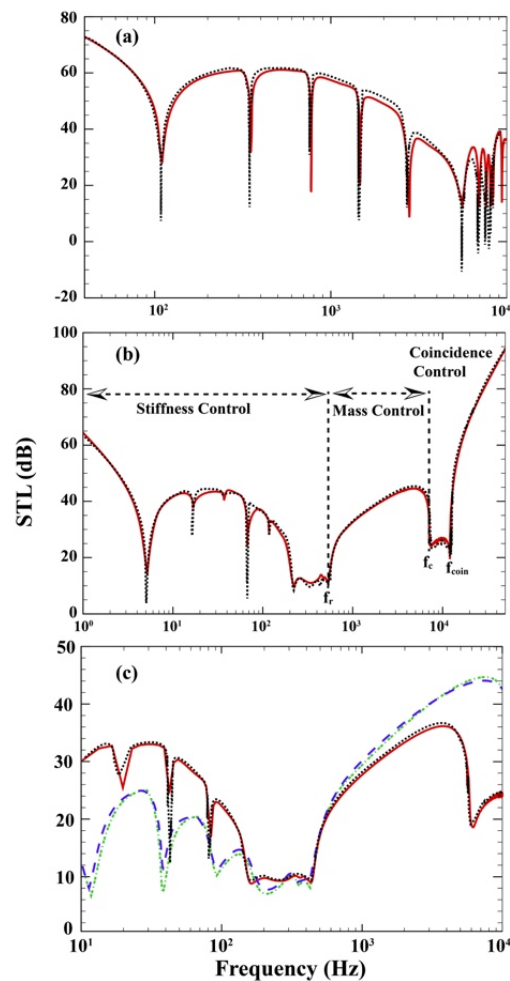


Figure 4. (a) Comparison study of STL curves for single elastic cylindrical shell, red solid line: present, black dotted line: Ref [55]. (b) Comparison study of STL for single elastic cylindrical shell, red solid line: present, black dotted line: Ref [71]. (c) Comparison study of STL for single elastic cylindrical shell under an external flow, red solid line: present ($M = 0$), black dotted line: Ref [63] ($M = 0$), purple dashed line: present ($M = 0.5$), green dashed-dotted line: Ref [63] ($M = 0.5$).

4.3. Parametric Study

Figure 5 shows the effect of incidence angles on the STL of a honeycomb sandwich cylindrical shell with FGP layers over a wide frequency range ($1 < f < 10^4$ Hz) when $R = 1.5\text{m}$, $h = 1\text{mm}$, $H = 5\text{mm}$, $\theta_c = \pi/6$, $l_c = 5\text{mm}$, $t_c = 0.5\text{mm}$, $p = 1$, $p_0 = 1\text{ Pa}$, $M = 0$, $\xi = 0$. STL plots are generally characterized by a set of frequencies that allow us to differentiate different behaviors observed in related acoustic problems. These frequencies, from the order of occurrence, are named ring, critical, and coincidence frequency (respectively denoted by f_r , f_{cr} , f_{co}). The reason behind the occurrence of such frequencies is described in detail in other studies [71,72]. However, it should be kept in mind that each interval formed by them gives rise to distinct phenomena. The frequencies lower than f_r form the stiffness-controlled region where the structural stiffness plays the most significant role in STL. In contrast, the mass-controlled region that starts from f_r and ends at f_{cr} is mostly affected by the structure's mass. Finally, the coincidence-controlled region lies above f_{co} . The value of f_{co} primarily depends on the incidence angle of sound waves. STL values and incidence angle are inversely proportional to each other. It is noteworthy that the STL valleys before the ring frequency are the shell resonances.

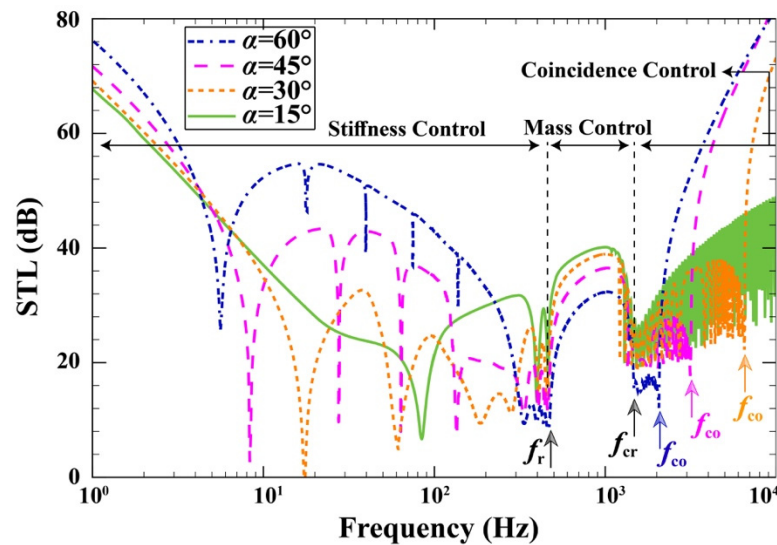


Figure 5. STL curves for different elevation angles.

As shown in Figure 6, the influence of material gradient index on the STL plots was investigated when $R = 1.5 \text{ m}$, $h = 1 \text{ mm}$, $H = 5 \text{ mm}$, $\theta_c = \frac{\pi}{6}$, $l_c = 5 \text{ mm}$, $t_c = 0.5 \text{ mm}$, $\alpha = \frac{\pi}{6}$, $p_0 = 1 \text{ Pa}$, $M = 0$, $\zeta = 0$. Figure 6 offers a good understanding of how to achieve higher levels of STL in different frequency regions. For example, reducing the FG index, i.e., attaining a stronger ceramic behavior instead of metallic behavior, is one way to increase STL in the stiffness-controlled region. The exact opposite is true for the mass-controlled region where reducing the FG index decreases STL. What is more, the characteristic frequencies can be shifted by changing the parameters of power law.

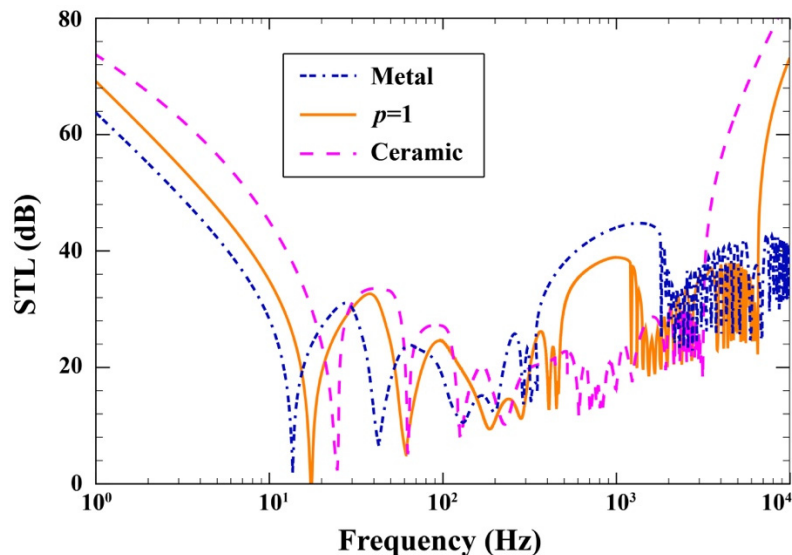


Figure 6. Variation of STL through the honeycomb FGP sandwich cylindrical shell with material gradient index.

To analyze the effect of the external flow Mach on the variations of STL curves, Figure 7 is presented, where $R = 1.5 \text{ m}$, $h = 1 \text{ mm}$, $H = 5 \text{ mm}$, $\theta_c = \frac{\pi}{6}$, $l_c = 5 \text{ mm}$, $t_c = 0.5 \text{ mm}$, $\alpha = \frac{\pi}{6}$, $p_0 = 1 \text{ Pa}$, $p = 1$, $\zeta = 0$. Another noteworthy finding is that the radiation damping after the ring frequency has the capability of increasing STL with a growing Mach number. In other words, a new value of Mach number results in different values of f_{cr} and f_{co} .

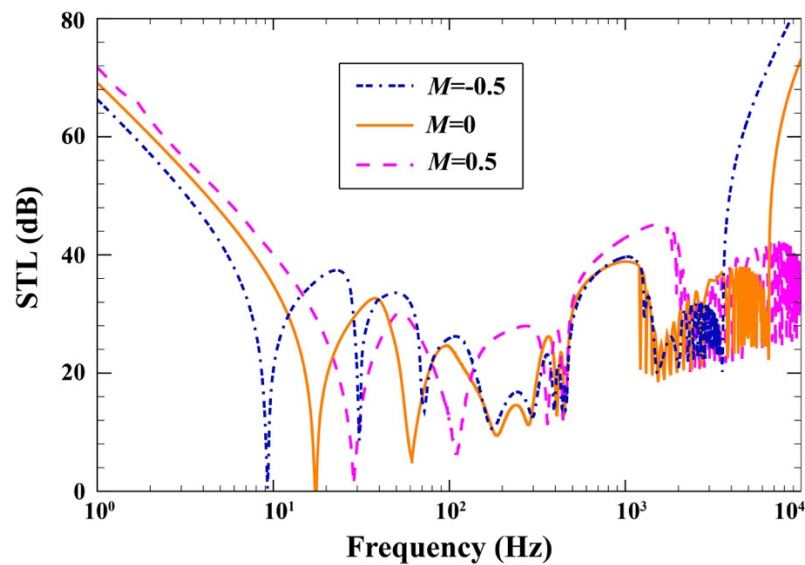


Figure 7. Effect of the external flow Mach number on the changes of STL.

Figure 8 depicts the effect of the average radius on the variations of STL curves when $M = 0$, $h = 1$ mm, $H = 5$ mm, $\theta_c = \frac{\pi}{6}$, $l_c = 5$ mm, $t_c = 0.5$ mm, $\alpha = \frac{\pi}{6}$, $p_0 = 1$ Pa, $p = 1$, $\zeta = 0$. It was expected to attain a lower STL for a larger radius before the ring frequency. In a stark contrast, changing the radius has virtually no effect on STL in the coincidence control region. This is due to the fact that at the high frequencies the wavelengths become shorter and therefore radius would incorporate no effect on STL in the coincidence control region. It should be noted that only the ring frequency is shifted as a result of a new radius.

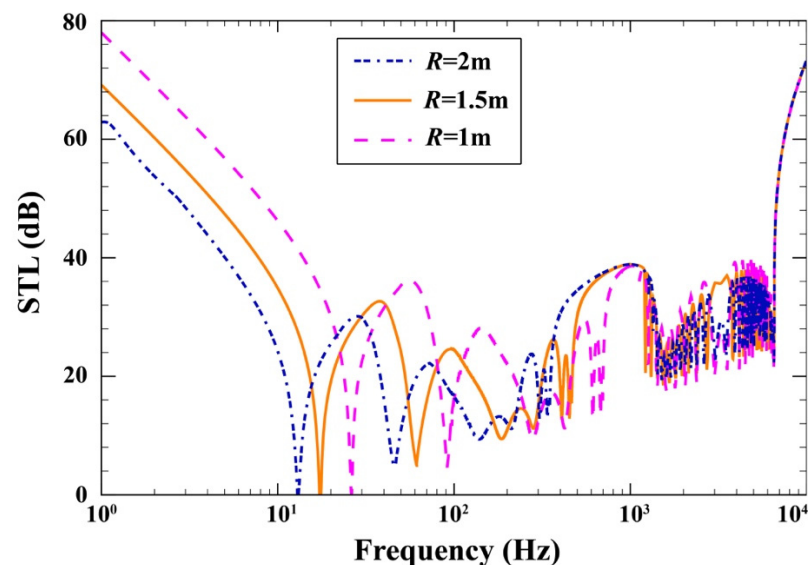


Figure 8. STL plots for different values of the average radius.

The variations of STL under different porosity distributions and porosity coefficient are indicated in Figure 9 when $M = 0$, $h = 1$ mm, $H = 5$ mm, $\theta_c = \frac{\pi}{6}$, $l_c = 5$ mm, $t_c = 0.5$ mm, $\alpha = \frac{\pi}{6}$, $p_0 = 1$ Pa, $p = 1$, $R = 1.5$. Turning our attention to the porosity coefficient, one observes a degraded STL performance with growing porosity coefficient irrespective of porosity pattern. To justify this behavior, one must pay attention to the decrease in the structural stiffness with growing porosity coefficient. This also explains the higher levels of STL for the case of logarithmic-uneven distribution as it possesses a higher stiffness than even porosity distribution. Nonetheless, for both porosity patterns, a

larger porosity coefficient shifts the critical and coincidence frequencies to the right of the frequency spectrum.

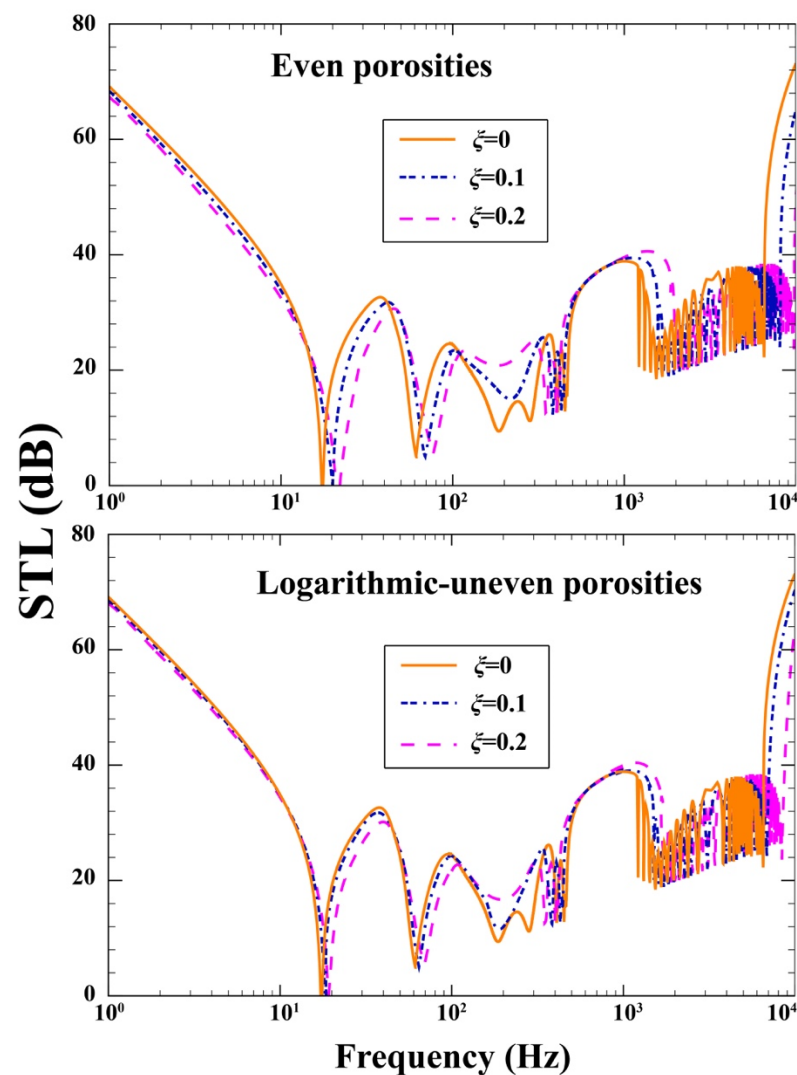


Figure 9. Effect of different porosity distributions and porosity coefficient on the changes of STL.

Figure 10 displays the effect of the wall thickness of honeycomb cell on the variations of STL over frequency range when $M = 0$, $h = 1$ mm, $H = 5$ mm, $\theta_c = \frac{\pi}{6}$, $l_c = 5$ mm, $\zeta = 0$, $\alpha = \frac{\pi}{6}$, $p_0 = 1$ Pa, $p = 1$, $R = 1.5$. The increase in the wall thickness of each honeycomb cell increases the core stiffness, so that STL grows. Furthermore, improvements in STL in the mass-controlled regions is observable.

Figure 11 demonstrates the variations of STL curves under different values of hexagonal cell length when $M = 0$, $h = 1$ mm, $H = 5$ mm, $\theta_c = \frac{\pi}{6}$, $t_c = 0.5$ mm, $\zeta = 0$, $\alpha = \frac{\pi}{6}$, $p_0 = 1$ Pa, $p = 1$, $R = 1.5$. Decreasing the value of l_c concurrently increases the elastic modulus, total bending stiffness, and structure's density. In addition, the total bending stiffness of the whole structure is decreased as a result of regulation impact, which increases STL in the stiffness-controlled and mass-controlled regions.

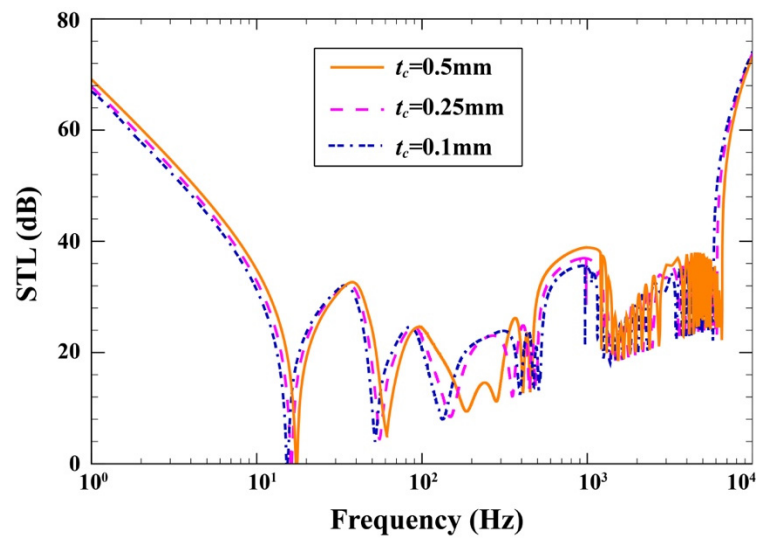


Figure 10. Effect of the wall thickness of honeycomb cell on the changes of STL.

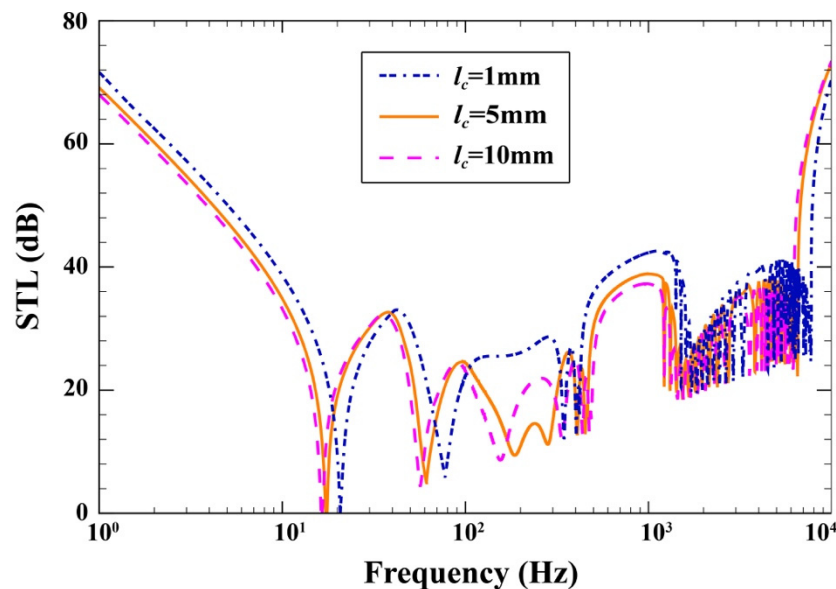


Figure 11. Effect of the hexagonal cell length on the changes of STL.

5. Conclusions

Using the FSDT as a capable means of investigating vibration problems, this article develops a formulation to determine the acousto-structural behavior of a sandwich structure incorporating a hexagonal honeycomb core and face layers made from FGP. A homogenous orthotropic model was used for the honeycomb core while its corresponding material features were found from the modified Gibson's equation. The distribution pattern of FGP parts is either even or logarithmic-uneven, and a special rule-of-mixture relation govern their properties. Then, fluid-structure compatibility relations were implemented followed by the use of Hamilton's principle, leading to the final form of governing equations. A series of simulations and comparisons with previous studies demonstrate the accuracy of the presented method. STL was then calculated over different frequency regions. The results are presented as follows:

- The increase in the wall thickness of each honeycomb cell increases the core stiffness, so that STL grows.

- Decreasing the value of l_c concurrently increases the elastic modulus, total bending stiffness, and structure's density, which increases STL in the stiffness-controlled and mass-controlled regions.
- STL reduces with growing porosity coefficient irrespective of porosity pattern.
- Higher levels of STL were obtained for the case of logarithmic-uneven distribution as it possesses a higher stiffness than even porosity distribution.
- Reducing the FG index, i.e., attaining a stronger ceramic behavior instead of metallic behavior, is one way to increase STL in the stiffness-controlled region.
- The radiation damping after f_r has the capability of increasing STL with a growing Mach number.

Author Contributions: Conceptualization, N.R., P.R.S. (Pouyan Roodgar Saffari) and S.K.; Data curation, C.T., T.J. and S.S.; Formal analysis, C.T., N.R., P.R.S. (Peyman Roudgar Saffari), P.R.S. (Pouyan Roodgar Saffari), S.S. and S.K.; Investigation, T.J., P.R.S. (Peyman Roudgar Saffari) and S.K.; Project administration, P.R.S. (Pouyan Roodgar Saffari); Resources, T.J., N.R. and S.S.; Software, C.T., T.J., N.R., P.R.S. (Peyman Roudgar Saffari), P.R.S. (Pouyan Roodgar Saffari), S.S. and S.K.; Supervision, C.T., P.R.S. (Pouyan Roodgar Saffari) and S.K.; Validation, C.T., T.J., N.R., P.R.S. (Peyman Roudgar Saffari), P.R.S. (Pouyan Roodgar Saffari), S.S. and S.K.; Visualization, C.T., N.R. and P.R.S. (Pouyan Roodgar Saffari); Writing—original draft, C.T. and P.R.S. (Peyman Roudgar Saffari); Writing—review & editing, P.R.S. (Peyman Roudgar Saffari) and S.S. All authors have read and agreed to the published version of the manuscript.

Funding: This research received no external funding.

Institutional Review Board Statement: Not applicable.

Informed Consent Statement: Not applicable.

Data Availability Statement: Data sharing not applicable.

Acknowledgments: This study was supported by the Thammasat Postdoctoral Fellowship, Thammasat University Research Division, Thammasat University. This Research was also supported by the Thammasat University Research Unit in Structural and Foundation Engineering, Thammasat University.

Conflicts of Interest: The authors declare no conflict of interest.

Appendix A

$$\delta U : a_{11} \frac{\partial^2 U}{\partial x^2} + b_{11} \frac{\partial^2 \phi_x}{\partial x^2} + a_{12} \frac{1}{R} \left(\frac{\partial^2 V}{\partial x \partial \theta} + \frac{\partial W}{\partial x} \right) + \frac{b_{12}}{R} \frac{\partial^2 \phi_\theta}{\partial x \partial \theta} + \frac{a_{66}}{R} \left(\frac{\partial^2 V}{\partial x \partial \theta} + \frac{1}{R} \frac{\partial^2 U}{\partial \theta^2} \right) + \frac{b_{66}}{R} \left(\frac{\partial^2 \phi_\theta}{\partial x \partial \theta} + \frac{1}{R} \frac{\partial^2 \phi_x}{\partial \theta^2} \right) = I_0 \frac{\partial^2 U}{\partial t^2} + I_1 \frac{\partial^2 \phi_x}{\partial t^2}, \quad (A1)$$

$$\delta V : a_{66} \left(\frac{\partial^2 V}{\partial x^2} + \frac{1}{R} \frac{\partial^2 U}{\partial x \partial \theta} \right) + b_{66} \left(\frac{\partial^2 \phi_\theta}{\partial x^2} + \frac{1}{R} \frac{\partial^2 \phi_x}{\partial x \partial \theta} \right) + \frac{a_{12}}{R} \frac{\partial^2 U}{\partial x \partial \theta} + \frac{b_{12}}{R} \frac{\partial^2 \phi_x}{\partial x \partial \theta} + \frac{a_{22}}{R} \frac{1}{R} \left(\frac{\partial^2 V}{\partial \theta^2} + \frac{\partial W}{\partial \theta} \right) + \frac{b_{22}}{R} \frac{1}{R} \frac{\partial^2 \phi_\theta}{\partial \theta^2} + \frac{k_s}{R} a_{44} \left(\phi_\theta + \frac{1}{R} \frac{\partial W}{\partial \theta} - \frac{V}{R} \right) = I_0 \frac{\partial^2 V}{\partial t^2} + I_1 \frac{\partial^2 \phi_\theta}{\partial t^2} \quad (A2)$$

$$\delta W : k_s a_{55} \left(\frac{\partial \phi_x}{\partial x} + \frac{\partial^2 W}{\partial x^2} \right) + \frac{k_s a_{44}}{R} \left(\frac{\partial \phi_\theta}{\partial \theta} + \frac{1}{R} \frac{\partial^2 W}{\partial \theta^2} - \frac{1}{R} \frac{\partial V}{\partial \theta} \right) - \frac{a_{12}}{R} \frac{\partial U}{\partial x} - \frac{b_{12}}{R} \frac{\partial \phi_x}{\partial x} - \frac{a_{22}}{R} \frac{1}{R} \left(\frac{\partial V}{\partial \theta} + W \right) - \frac{b_{22}}{R} \frac{\partial \phi_\theta}{\partial \theta} = I_0 \frac{\partial^2 W}{\partial t^2} - \Delta P, \quad (A3)$$

$$\delta \phi_x : b_{11} \frac{\partial^2 U}{\partial x^2} + d_{11} \frac{\partial^2 \phi_x}{\partial x^2} + b_{12} \frac{1}{R} \left(\frac{\partial^2 V}{\partial x \partial \theta} + \frac{\partial W}{\partial x} \right) + \frac{d_{12}}{R} \frac{\partial^2 \phi_\theta}{\partial x \partial \theta} + \frac{b_{66}}{R} \left(\frac{\partial^2 V}{\partial x \partial \theta} + \frac{1}{R} \frac{\partial^2 U}{\partial \theta^2} \right) + \frac{d_{66}}{R} \left(\frac{\partial^2 \phi_\theta}{\partial x \partial \theta} + \frac{1}{R} \frac{\partial^2 \phi_x}{\partial \theta^2} \right) - k_s a_{55} \left(\phi_x + \frac{\partial W}{\partial x} \right) = I_1 \frac{\partial^2 U}{\partial t^2} + I_2 \frac{\partial^2 \phi_x}{\partial t^2}, \quad (A4)$$

$$\delta \phi_\theta : b_{66} \left(\frac{\partial^2 V}{\partial x^2} + \frac{1}{R} \frac{\partial^2 U}{\partial x \partial \theta} \right) + d_{66} \left(\frac{\partial^2 \phi_\theta}{\partial x^2} + \frac{1}{R} \frac{\partial^2 \phi_x}{\partial x \partial \theta} \right) + \frac{b_{12}}{R} \frac{\partial^2 U}{\partial x \partial \theta} + \frac{d_{12}}{R} \frac{\partial^2 \phi_x}{\partial x \partial \theta} + \frac{b_{22}}{R} \frac{1}{R} \left(\frac{\partial^2 V}{\partial \theta^2} + \frac{\partial W}{\partial \theta} \right) + \frac{d_{22}}{R} \frac{1}{R} \frac{\partial^2 \phi_\theta}{\partial \theta^2} - k_s a_{44} \left(\phi_\theta + \frac{1}{R} \frac{\partial W}{\partial \theta} - \frac{V}{R} \right) = I_1 \frac{\partial^2 V}{\partial t^2} + I_2 \frac{\partial^2 \phi_\theta}{\partial t^2}, \quad (A5)$$

where

$$\begin{aligned}
[a_{11}, b_{11}, d_{11}] &= \int_{-\frac{H}{2}-h}^{-\frac{H}{2}} \frac{E^B(z)}{1-\theta^B(z)\theta^B(z)} [1, z, z^2] dz + \int_{-\frac{H}{2}}^{\frac{H}{2}} \frac{E_1^C}{1-\theta_{12}^C\theta_{21}^C} [1, z, z^2] dz + \int_{\frac{H}{2}}^{\frac{H}{2}+h} \frac{E^T(z)}{1-\theta^T(z)\theta^T(z)} [1, z, z^2] dz, \\
[a_{12}, b_{12}, d_{12}] &= \int_{-\frac{H}{2}-h}^{-\frac{H}{2}} \frac{\theta(z)E^B(z)}{1-\theta^B(z)\theta^B(z)} [1, z, z^2] dz + \int_{-\frac{H}{2}}^{\frac{H}{2}} \frac{\theta_{12}^C E_2^C}{1-\theta_{12}^C\theta_{21}^C} [1, z, z^2] dz + \int_{\frac{H}{2}}^{\frac{H}{2}+h} \frac{\theta(z)E^T(z)}{1-\theta^T(z)\theta^T(z)} [1, z, z^2] dz, \\
[a_{22}, b_{22}, d_{22}] &= \int_{-\frac{H}{2}-h}^{-\frac{H}{2}} \frac{E^B(z)}{1-\theta^B(z)\theta^B(z)} [1, z, z^2] dz + \int_{-\frac{H}{2}}^{\frac{H}{2}} \frac{E_2^C}{1-\theta_{12}^C\theta_{21}^C} [1, z, z^2] dz + \int_{\frac{H}{2}}^{\frac{H}{2}+h} \frac{E^T(z)}{1-\theta^T(z)\theta^T(z)} [1, z, z^2] dz, \\
a_{44} &= \int_{-\frac{H}{2}-h}^{-\frac{H}{2}} \frac{E^B(z)}{2(1+\theta^B(z))} dz + \int_{-\frac{H}{2}}^{\frac{H}{2}} G_{23}^C dz + \int_{\frac{H}{2}}^{\frac{H}{2}+h} \frac{E^T(z)}{2(1+\theta^T(z))} dz, \\
a_{55} &= \int_{-\frac{H}{2}-h}^{-\frac{H}{2}} \frac{E^B(z)}{2(1+\theta^B(z))} dz + \int_{-\frac{H}{2}}^{\frac{H}{2}} G_{13}^C dz + \int_{\frac{H}{2}}^{\frac{H}{2}+h} \frac{E^T(z)}{2(1+\theta^T(z))} dz, \\
[a_{66}, d_{66}] &= \int_{-\frac{H}{2}-h}^{-\frac{H}{2}} \frac{E^B(z)}{2(1+\theta^B(z))} [1, z^2] dz + \int_{-\frac{H}{2}}^{\frac{H}{2}} G_{12}^C [1, z^2] dz + \int_{\frac{H}{2}}^{\frac{H}{2}+h} G_{12}^C [1, z^2] dz,
\end{aligned}$$

Appendix B

$$\begin{aligned}
Y_{1,3} &= -\left(a_{11}k_x^2 + \frac{a_{66}}{R^2}n^2\right) + I_0\omega^2, \\
Y_{1,4} &= Y_{2,3} = -\frac{1}{R}k_x n(a_{12} + a_{66}), \\
Y_{1,5} &= -Y_{3,3} = -\frac{1}{R}k_x a_{12}, \\
Y_{1,6} &= Y_{4,3} = -\left(b_{11}k_x^2 + \frac{b_{66}}{R^2}n^2\right) + I_1\omega^2, \\
Y_{1,7} &= Y_{5,3} = -\frac{1}{R}k_x n(b_{12} + b_{66}), \\
Y_{2,4} &= -\left(a_{66}k_x^2 + \frac{a_{22}}{R^2}n^2 + \frac{k_s a_{44}}{R^2}\right) + I_0\omega^2, \\
Y_{2,5} &= Y_{3,4} = -\left(\frac{a_{22}}{R^2}n + \frac{k_s a_{44}}{R^2}n\right), \\
Y_{2,6} &= Y_{4,4} = -\frac{1}{R}k_x n(b_{12} + b_{66}), \\
Y_{2,7} &= Y_{5,4} = -\left(b_{66}k_x^2 + \frac{b_{22}}{R^2}n^2 - \frac{k_s a_{44}}{R}\right) + I_1\omega^2, \\
Y_{3,1} &= H_n^{(2)}(k_{1r}R), \\
Y_{3,2} &= -H_n^{(1)}(k_{2r}R), \\
Y_{3,5} &= -\left(k_x^2 k_s a_{55} + \frac{k_s a_{44}}{R^2}n^2 + \frac{a_{22}}{R^2}\right) + I_0\omega^2, \\
Y_{3,6} &= -Y_{4,5} = -\left(ik_x k_s a_{55} - ik_x \frac{b_{12}}{R}\right), \\
Y_{3,7} &= Y_{5,5} = \left(\frac{k_s a_{44}}{R}n - \frac{b_{22}}{R^2}n\right), \\
f_3 &= -p_0 \varepsilon_n (-i)^n J_n(k_{1r}R), \\
Y_{4,6} &= -\left(k_x^2 d_{11} + \frac{d_{66}}{R^2}n^2 + k_s a_{55}\right) + I_2\omega^2, \\
Y_{4,7} &= Y_{5,6} = -ik_x \frac{1}{R}n(d_{12} + d_{66}), \\
Y_{5,7} &= -\left(\frac{d_{22}}{R^2}n^2 + k_x^2 d_{66} + k_s a_{44}\right) + I_2\omega^2, \\
Y_{6,1} &= k_{1r} H_n^{(2)'}(k_{1r}R), \\
Y_{6,5} &= -\rho_0(\omega - \mathcal{V}k_x)^2, \\
f_6 &= -p_0 \varepsilon_n (-i)^n k_{1r} J_n'(k_{1r}R), \\
Y_{7,2} &= k_{2r} H_n^{(1)'}(k_{2r}R), \\
Y_{7,5} &= -\rho_0\omega^2,
\end{aligned}$$

References

- Funari, M.F.; Spadea, S.; Lonetti, P.; Lourenço, P.B. On the elastic and mixed-mode fracture properties of PVC foam. *Theor. Appl. Fract. Mech.* **2021**, *112*, 102924. [\[CrossRef\]](#)
- Funari, M.F.; Greco, F.; Lonetti, P. Sandwich panels under interfacial debonding mechanisms. *Compos. Struct.* **2018**, *203*, 310–320. [\[CrossRef\]](#)
- Atas, C.; Sevim, C. On the impact response of sandwich composites with cores of balsa wood and PVC foam. *Compos. Struct.* **2010**, *93*, 40–48. [\[CrossRef\]](#)
- Bruno, D.; Fabbrocino, F.; Funari, M.F.; Greco, F.; Lonetti, P.; Spadea, S. An Experimental and Numerical Study to Evaluate the Crack Path Under Mixed Mode Loading on Pvc Foams. In *Conference of the Italian Association of Theoretical and Applied Mechanics*; Springer: Berlin/Heidelberg, Germany, 2019; pp. 378–388.

5. Balcı, O.; Çoban, O.; Bora, M.Ö.; Akagündüz, E.; Yalçın, E.B. Experimental investigation of single and repeated impacts for repaired honeycomb sandwich structures. *Mater. Sci. Eng. A* **2017**, *682*, 23–30. [[CrossRef](#)]
6. Li, Y.; Jin, Z. Free flexural vibration analysis of symmetric rectangular honeycomb panels with SCSC edge supports. *Compos. Struct.* **2008**, *83*, 154–158. [[CrossRef](#)]
7. Yongqiang, L.; Feng, L.; Dawei, Z. Geometrically nonlinear free vibrations of the symmetric rectangular honeycomb sandwich panels with simply supported boundaries. *Compos. Struct.* **2010**, *92*, 1110–1119. [[CrossRef](#)]
8. Duc, N.D.; Seung-Eock, K.; Tuan, N.D.; Tran, P.; Khoa, N.D. New approach to study nonlinear dynamic response and vibration of sandwich composite cylindrical panels with auxetic honeycomb core layer. *Aerosp. Sci. Technol.* **2017**, *70*, 396–404. [[CrossRef](#)]
9. Duc, N.D.; Seung-Eock, K.; Cong, P.H.; Anh, N.T.; Khoa, N.D. Dynamic response and vibration of composite double curved shallow shells with negative Poisson's ratio in auxetic honeycombs core layer on elastic foundations subjected to blast and damping loads. *Int. J. Mech. Sci.* **2017**, *133*, 504–512. [[CrossRef](#)]
10. Li, Y.; Yao, W.; Wang, T. Free flexural vibration of thin-walled honeycomb sandwich cylindrical shells. *Thin-Walled Struct.* **2020**, *157*, 107032. [[CrossRef](#)]
11. Eipakchi, H.; Nasrekani, F.M. Vibrational behavior of composite cylindrical shells with auxetic honeycombs core layer subjected to a moving pressure. *Compos. Struct.* **2020**, *254*, 112847. [[CrossRef](#)]
12. Van Quyen, N.; Van Thanh, N.; Quan, T.Q.; Duc, N.D. Nonlinear forced vibration of sandwich cylindrical panel with negative Poisson's ratio auxetic honeycombs core and CNTRC face sheets. *Thin-Walled Struct.* **2021**, *162*, 107571. [[CrossRef](#)]
13. Koval, L.R. On sound transmission into a thin cylindrical shell under “flight conditions”. *J. Sound Vib.* **1976**, *48*, 265–275. [[CrossRef](#)]
14. Lee, J.-H.; Kim, J. Analysis and measurement of sound transmission through a double-walled cylindrical shell. *J. Sound Vib.* **2002**, *251*, 631–649. [[CrossRef](#)]
15. Talebitooti, R.; Choudari Khameneh, A.M.; Zarastvand, M.R.; Kornokar, M. Investigation of three-dimensional theory on sound transmission through compressed poroelastic sandwich cylindrical shell in various boundary configurations. *J. Sandw. Struct. Mater.* **2019**, *21*, 2313–2357. [[CrossRef](#)]
16. Daneshjou, K.; Nouri, A.; Talebitooti, R. Sound transmission through laminated composite cylindrical shells using analytical model. *Arch. Appl. Mech.* **2007**, *77*, 363–379. [[CrossRef](#)]
17. Kerboua, Y.; Lakis, A.A. Numerical model to analyze the aerodynamic behavior of a combined conical–cylindrical shell. *Aerosp. Sci. Technol.* **2016**, *58*, 601–617. [[CrossRef](#)]
18. Ebrahimi, F.; Hashemabadi, D.; Habibi, M.; Safarpour, H. Thermal buckling and forced vibration characteristics of a porous GNP reinforced nanocomposite cylindrical shell. *Microsyst. Technol.* **2020**, *26*, 461–473. [[CrossRef](#)]
19. Thongchom, C.; Refahati, N.; Saffari, P.R.; Saffari, P.R.; Niyaraki, M.N.; Sirimontree, S.; Keawsawasvong, S. An Experimental Study on the Effect of Nanomaterials and Fibers on the Mechanical Properties of Polymer Composites. *Buildings* **2022**, *12*, 7. [[CrossRef](#)]
20. Deng, J.; Guasch, O.; Maxit, L.; Zheng, L. Vibration of cylindrical shells with embedded annular acoustic black holes using the Rayleigh-Ritz method with Gaussian basis functions. *Mech. Syst. Signal Process.* **2021**, *150*, 107225. [[CrossRef](#)]
21. Roodgar Saffari, P.; Fakhraie, M.; Roudbari, M.A. Free vibration problem of fluid-conveying double-walled boron nitride nanotubes via nonlocal strain gradient theory in thermal environment. *Mech. Based Des. Struct. Mach.* **2020**, 1–18. [[CrossRef](#)]
22. Zarabimaneh, Y.; Roodgar Saffari, P.; Roudgar Saffari, P.; Refahati, N. Hygro-thermo-mechanical vibration of two vertically aligned single-walled boron nitride nanotubes conveying fluid. *J. Vib. Control* **2021**. [[CrossRef](#)]
23. Roodgar Saffari, P.; Fakhraie, M.; Roudbari, M.A. Size-Dependent Vibration Problem of Two Vertically-Aligned Single-Walled Boron Nitride Nanotubes Conveying Fluid in Thermal Environment Via Nonlocal Strain Gradient Shell Model. *J. Solid Mech.* **2021**, *13*, 164–185.
24. Saffari, P.R.; Fakhraie, M.; Roudbari, M.A. Nonlinear vibration of fluid conveying cantilever nanotube resting on visco-pasternak foundation using non-local strain gradient theory. *Micro. Nano Lett.* **2020**, *15*, 181–186. [[CrossRef](#)]
25. Hosseini, M.; Jamalpoor, A. Analytical Solution for Thermomechanical Vibration of Double-Viscoelastic Nanoplate-Systems Made of Functionally Graded Materials. *J. Therm. Stress* **2015**, *38*, 1428–1456. [[CrossRef](#)]
26. Mahamood, R.M.; Akinlabi, E.T.; Shukla, M.; Pityana, S. Functionally Graded Material: An Overview. In Proceedings of the World Congress on Engineering 2012 Vol III (WCE 2012), London, UK, 4–6 July 2012.
27. Belabed, Z.; Houari, M.S.A.; Tounsi, A.; Mahmoud, S.R.; Bég, O.A. An efficient and simple higher order shear and normal deformation theory for functionally graded material (FGM) plates. *Compos. Part. B Eng.* **2012**, *60*, 274–283. [[CrossRef](#)]
28. Hosseini, M.; Jamalpoor, A.; Fath, A. Surface effect on the biaxial buckling and free vibration of FGM nanoplate embedded in visco-Pasternak standard linear solid-type of foundation. *Meccanica* **2017**, *52*, 1381–1396. [[CrossRef](#)]
29. Hosseini, M.; Bahreman, M.; Jamalpoor, A. Thermomechanical vibration analysis of FGM viscoelastic multi-nanoplate system incorporating the surface effects via nonlocal elasticity theory. *Microsyst. Technol.* **2017**, *23*, 3041–3058. [[CrossRef](#)]
30. Roodgar Saffari, P.; Fakhraie, M.; Roudbari, M.A. Free Vibration and Transient Response of Heterogeneous Piezoelectric Sandwich Annular Plate Using Third-Order Shear Deformation Assumption. *J. Solid Mech.* **2020**, *12*, 315–333. [[CrossRef](#)]
31. Kato, K.; Kurimoto, M.; Shumiya, H.; Adachi, H.; Sakuma, S.; Okubo, H. Application of functionally graded material for solid insulator in gaseous insulation system. *IEEE Trans. Dielectr. Electr. Insul.* **2006**, *13*, 362–372. [[CrossRef](#)]

32. Sinha, G.P.; Kumar, B. Review on vibration analysis of functionally graded material structural components with cracks. *J. Vib. Eng. Technol.* **2021**, *9*, 23–49. [[CrossRef](#)]
33. Yılmaz, E.; Kabataş, F.; Gökçe, A.; Fındık, F. Production and Characterization of a Bone-Like Porous Ti/Ti-Hydroxyapatite Functionally Graded Material. *J. Mater. Eng. Perform.* **2020**, *29*, 6455–6467. [[CrossRef](#)]
34. Loy, C.T.; Lam, K.Y.; Reddy, J.N. Vibration of functionally graded cylindrical shells. *Int. J. Mech. Sci.* **1999**, *41*, 309–324. [[CrossRef](#)]
35. Pradhan, S.C.; Loy, C.T.; Lam, K.Y.; Reddy, J.N. Vibration characteristics of functionally graded cylindrical shells under various boundary conditions. *Appl. Acoust.* **2000**, *61*, 111–129. [[CrossRef](#)]
36. Liu, T.; Wang, A.; Wang, Q.; Qin, B. Wave based method for free vibration characteristics of functionally graded cylindrical shells with arbitrary boundary conditions. *Thin-Walled Struct.* **2020**, *148*, 106580. [[CrossRef](#)]
37. Wang, Y.; Ye, C.; Zu, J.W. Identifying the temperature effect on the vibrations of functionally graded cylindrical shells with porosities. *Appl. Math. Mech.* **2018**, *39*, 1587–1604. [[CrossRef](#)]
38. Baghlani, A.; Khayat, M.; Dehghan, S.M. Free vibration analysis of FGM cylindrical shells surrounded by Pasternak elastic foundation in thermal environment considering fluid-structure interaction. *Appl. Math. Model.* **2020**, *78*, 550–575. [[CrossRef](#)]
39. Sofiyev, A.H. Dynamic response of an FGM cylindrical shell under moving loads. *Compos. Struct.* **2010**, *93*, 58–66. [[CrossRef](#)]
40. Baghbadorani, A.A.; Kiani, Y. Free vibration analysis of functionally graded cylindrical shells reinforced with graphene platelets. *Compos. Struct.* **2021**, *276*, 114546. [[CrossRef](#)]
41. Nguyen, T.P.; Nguyen-Thoi, T.; Tran, D.K.; Ho, D.T.; Vu, H.N. Nonlinear vibration of full-filled fluid corrugated sandwich functionally graded cylindrical shells. *J. Vib. Control* **2021**, *27*, 1020–1035. [[CrossRef](#)]
42. Ni, Y.; Zhu, S.; Sun, J.; Tong, Z.; Zhou, Z.; Xu, X.; Lim, C.W. An accurate model for free vibration of porous magneto-electro-thermo-elastic functionally graded cylindrical shells subjected to multi-field coupled loadings. *J. Intell. Mater. Syst. Struct.* **2021**, *32*, 2006–2023. [[CrossRef](#)]
43. Cong, P.H.; Duc, N.D. Nonlinear thermo-mechanical analysis of ES double curved shallow auxetic honeycomb sandwich shells with temperature-dependent properties. *Compos. Struct.* **2021**, *279*, 114739. [[CrossRef](#)]
44. Rodriguez-Castro, R.; Wetherhold, R.C.; Kelestemur, M.H. Microstructure and mechanical behavior of functionally graded Al A359/SiCp composite. *Mater. Sci. Eng. A* **2002**, *323*, 445–456. [[CrossRef](#)]
45. Wang, Y.; Wu, D. Free vibration of functionally graded porous cylindrical shell using a sinusoidal shear deformation theory. *Aerosp. Sci. Technol.* **2017**, *66*, 83–91. [[CrossRef](#)]
46. Cuong-Le, T.; Nguyen, K.D.; Nguyen-Trong, N.; Khatir, S.; Nguyen-Xuan, H.; Abdel-Wahab, M. A three-dimensional solution for free vibration and buckling of annular plate, conical, cylinder and cylindrical shell of FG porous-cellular materials using IGA. *Compos. Struct.* **2021**, *259*, 113216. [[CrossRef](#)]
47. Shahgholian, D.; Safarpour, M.; Rahimi, A.R.; Alibeigloo, A. Buckling analyses of functionally graded graphene-reinforced porous cylindrical shell using the Rayleigh–Ritz method. *Acta Mech.* **2020**, *231*, 1887–1902. [[CrossRef](#)]
48. Ghadiri, M.; Safar Pour, H. Free vibration analysis of size-dependent functionally graded porous cylindrical microshells in thermal environment. *J. Therm. Stress* **2017**, *40*, 55–71. [[CrossRef](#)]
49. Keleshteri, M.M.; Jelovica, J. Nonlinear vibration behavior of functionally graded porous cylindrical panels. *Compos. Struct.* **2020**, *239*, 112028. [[CrossRef](#)]
50. Li, Z.; Zhong, R.; Wang, Q.; Qin, B.; Yu, H. The thermal vibration characteristics of the functionally graded porous stepped cylindrical shell by using characteristic orthogonal polynomials. *Int. J. Mech. Sci.* **2020**, *182*, 105779. [[CrossRef](#)]
51. Hasheminejad, S.M.; Jamalpoor, A. Sound transmission control through a hybrid smart double sandwich plate structure. *J. Sandw. Struct. Mater.* **2021**, *23*, 2443–2483. [[CrossRef](#)]
52. Heckl, M. The tenth Sir Richard Fairey memorial lecture: Sound transmission in buildings. *J. Sound Vib.* **1981**, *77*, 165–189. [[CrossRef](#)]
53. Pellicier, A.; Trompette, N. A review of analytical methods, based on the wave approach, to compute partitions transmission loss. *Appl. Acoust.* **2007**, *68*, 1192–1212. [[CrossRef](#)]
54. Ramezani, H.; Talebitooti, R. Vibroacoustic response of a double-walled cylindrical FGM shell with a porous sandwiched layer. *Mech. Compos. Mater.* **2015**, *51*, 581–592. [[CrossRef](#)]
55. Daneshjou, K.; Talebitooti, R.; Tarkashvand, A. Analysis of sound transmission loss through thick-walled cylindrical shell using three-dimensional elasticity theory. *Int. J. Mech. Sci.* **2016**, *106*, 286–296. [[CrossRef](#)]
56. Oliazadeh, P.; Farshidianfar, A. Analysis of different techniques to improve sound transmission loss in cylindrical shells. *J. Sound Vib.* **2017**, *389*, 276–291. [[CrossRef](#)]
57. Ahmadi, M.; Talebitooti, M.; Talebitooti, R. Analytical investigation on sound transmission loss of functionally graded nanocomposite cylindrical shells reinforced by carbon nanotubes. *Mech. Based Des. Struct. Mach.* **2020**, 1–18. [[CrossRef](#)]
58. Hasheminejad, S.M.; Cheraghi, M.; Jamalpoor, A. Active damping of sound transmission through an electrorheological fluid-actuated sandwich cylindrical shell. *J. Sandw. Struct. Mater.* **2020**, *22*, 833–865. [[CrossRef](#)]
59. Fu, T.; Wu, X.; Xiao, Z.; Chen, Z. Thermoacoustic response of porous FGM cylindrical shell surround by elastic foundation subjected to nonlinear thermal loading. *Thin-Walled Struct.* **2020**, *156*, 106996. [[CrossRef](#)]
60. Hasheminejad, S.M.; Jamalpoor, A. Control of sound transmission into a hybrid double-wall sandwich cylindrical shell. *J. Vib. Control* **2021**. [[CrossRef](#)]

61. Li, F.; Yuan, W.; Zhang, C. Free vibration and sound insulation of functionally graded honeycomb sandwich plates. *J. Sandw. Struct. Mater.* **2021**, *24*, 565–600. [[CrossRef](#)]
62. Daneshjou, K.; Nouri, A.; Talebitooti, R. Analytical model of sound transmission through orthotropic cylindrical shells with subsonic external flow. *Aerosp. Sci. Technol.* **2009**, *13*, 18–26. [[CrossRef](#)]
63. Zhou, J.; Bhaskar, A.; Zhang, X. The effect of external mean flow on sound transmission through double-walled cylindrical shells lined with poroelastic material. *J. Sound Vib.* **2014**, *333*, 1972–1990. [[CrossRef](#)]
64. Hosseini, M.; Mofidi, M.R.; Jamalpoor, A.; Jahanshahi, M.S. Nanoscale mass nanosensor based on the vibration analysis of embedded magneto-electro-elastic nanoplate made of FGMs via nonlocal Mindlin plate theory. *Microsyst. Technol.* **2018**, *24*, 2295–2316. [[CrossRef](#)]
65. Kreja, I.; Schmidt, R.; Reddy, J.N. Finite elements based on a first-order shear deformation moderate rotation shell theory with applications to the analysis of composite structures. *Int. J. Non Linear Mech.* **1997**, *32*, 1123–1142. [[CrossRef](#)]
66. Amabili, M. *Nonlinear Vibrations and Stability of Shells and Plates*; Cambridge University Press: Cambridge, UK, 2008.
67. Liu, Y.; He, C. Diffuse field sound transmission through sandwich composite cylindrical shells with poroelastic core and external mean flow. *Compos. Struct.* **2016**, *135*, 383–396. [[CrossRef](#)]
68. Kiani, A.; Sheikhhoshkar, M.; Jamalpoor, A.; Khanzadi, M. Free vibration problem of embedded magneto-electro-thermo-elastic nanoplate made of functionally graded materials via nonlocal third-order shear deformation theory. *J. Intell Mater. Syst. Struct.* **2018**, *29*, 741–763. [[CrossRef](#)]
69. Nikrad, S.F.; Kanellopoulos, A.; Bodaghi, M.; Chen, Z.T.; Poursasghar, A. Large deformation behavior of functionally graded porous curved beams in thermal environment. *Arch. Appl. Mech.* **2021**, *91*, 2255–2278. [[CrossRef](#)]
70. Hasheminejad, S.M.; Jamalpoor, A. Cancellation of acoustic scattering from a smart hybrid ERF/PZT-based double-wall composite spherical shell structure. *Mech. Adv. Mater. Struct.* **2021**, 1–22. [[CrossRef](#)]
71. Talebitooti, R.; Zarastvand, M.R.; Gheibi, M.R. Acoustic transmission through laminated composite cylindrical shell employing Third order Shear Deformation Theory in the presence of subsonic flow. *Compos. Struct.* **2016**, *157*, 95–110. [[CrossRef](#)]
72. Reaei, S.; Tarkashvand, A.; Talebitooti, R. Applying a functionally graded viscoelastic model on acoustic wave transmission through the polymeric foam cylindrical shell. *Compos. Struct.* **2020**, *244*, 112261. [[CrossRef](#)]